Local and symmetry-resolved electronic structure of liquid dimethyl sulfoxide from resonant inelastic soft x-ray scattering

Lothar Weinhardt[1,2,3,], Dirk Hauschild[1,2,3], Ralph Steininger[1], Constantin Wansorra[1,3], Wanli Yang[4], and Clemens Heske[1,2,3]*

[1]Institute for Photon Science and Synchrotron Radiation (IPS), Karlsruhe Institute of Technology (KIT), Kaiserstr. 12, 76131 Karlsruhe, Germany

[2]Institute for Chemical Technology and Polymer Chemistry (ITCP), Karlsruhe Institute of Technology (KIT), Kaiserstr. 12, 76131 Karlsruhe, Germany

[3]Department of Chemistry and Biochemistry, University of Nevada, Las Vegas (UNLV), 4505 Maryland Parkway, Las Vegas, NV 89154, USA

[4]Advanced Light Source (ALS), Lawrence Berkeley National Laboratory, 1 Cyclotron Road, Berkeley, CA 94720, USA
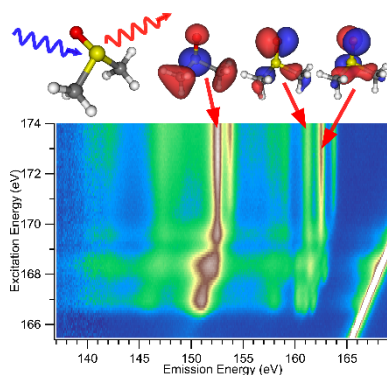

AUTHOR INFORMATION

Corresponding Author

*(L.W.) E-mail: Lothar.Weinhardt@kit.edu

ABSTRACT

Dimethyl sulfoxide (DMSO) is an important polar solvent that derives its unique properties from the lone pair and strongly polar bond at the sulfinyl functional group. To derive the local and symmetry-resolved electronic structure of liquid DMSO, we have used resonant inelastic soft x-ray scattering (RIXS) maps at the S $L_{2,3}$, C K, and O K edges. The experimental data is compared to spectra calculations based on density functional theory, which allows a detailed analysis of the molecular orbitals throughout the molecule. In the RIXS maps, we find the signature of molecular-field splitting of the S 2p core levels, vibronic coupling, and ultra-fast nuclear dynamics on the timescale of the RIXS process.
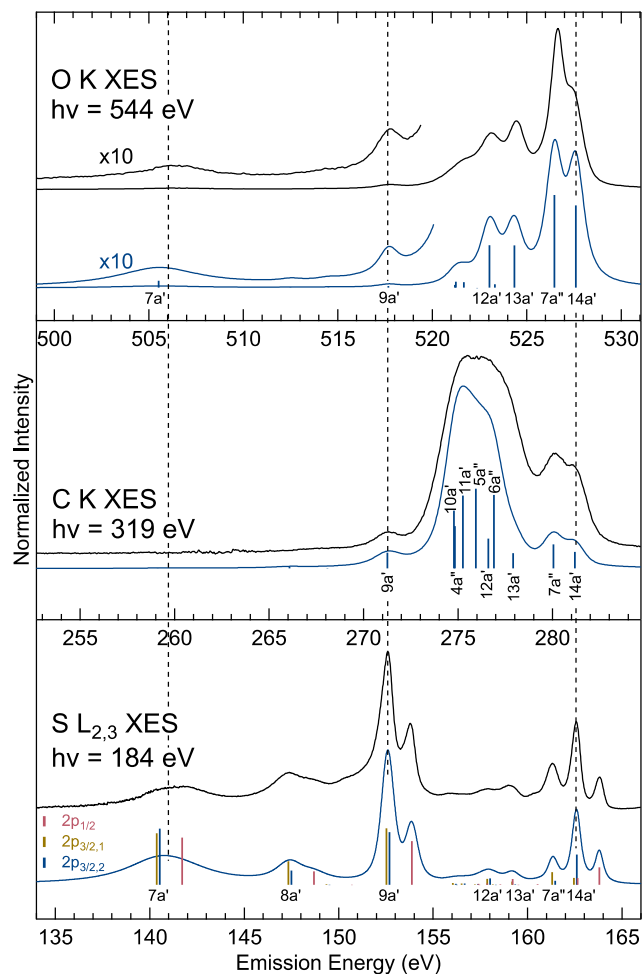
TOC GRAPHICS

KEYWORDS DMSO, polar solvent, molecular orbitals, density functional theory, molecular field splitting, ultrafast nuclear dynamics, resonant inelastic soft x-ray scattering, RIXS

Dimethyl sulfoxide (DMSO) is a commonly used highly polar solvent. It dissolves a wide range of both polar and non-polar organic and inorganic compounds, and has a comparatively low toxicity, which has led to its wide-spread use. DMSO has a trigonal pyramidal structure (see Figure S1) with a lone pair at the sulfur atom. Its advantageous properties are strongly defined by the sulfinyl functional group, in which the nature of the bond between sulfur and oxygen plays a crucial role. This bond has been intensively investigated, mostly based on density functional theory (DFT) calculations, and described with both double-bond and zwitterionic characteristics[1–3]. On the experimental side, the structure of liquid DMSO has been studied using x-ray and neutron diffraction[4,5] as well as NMR spectroscopy[3].

To probe the *electronic* structure of DMSO, x-ray spectroscopy in the hard[6,7] and soft[6,8–12] x-ray range has been employed. In an early pioneering study by Sze et al.[6], the x-ray absorption (XAS) spectra of gas phase DMSO were collected at the S $L_{2,3}$, S L_1, C K, O K, and S K edges with a first tentative assignment of spectral features. In a recent S K XAS study, combined with density functional theory (DFT) spectra calculations, a signature of hydrogen bonding in liquid DMSO was observed[7]. All other recent soft x-ray studies used XAS, x-ray emission spectroscopy (XES), and/or resonant inelastic x-ray scattering (RIXS) *at the O K edge*, to probe different aspects of DMSO from the viewpoint of the sulfinyl oxygen. O K RIXS studies of pure liquid DMSO focused on the S-O bond[8] as well as the molecular orbital symmetry, exploiting the angular anisotropy of RIXS[10]. Furthermore, the hydrogen-bonding network in DMSO/water mixtures was investigated using XAS[9,12] and RIXS[9].

In the present study, we probe *all accessible sites* of the molecule by employing RIXS (as well as non-resonant XES) at the S $L_{2,3}$, C K, *and* O K edges, in combination with DFT calculations, to derive the first complete picture of the electronic structure of liquid DMSO.

The understand the spectral features in our RIXS maps, we first discuss the experimental non-resonant O K, C K, and S $L_{2,3}$ XES spectra (black) of DMSO in Figure 1, together with DFT-based spectra simulations (blue). Calculated intensities and energies of the individual transitions are shown as colored vertical lines, while the continuous blue spectrum was calculated after broadening with Voigt line profiles. The Gaussian widths were kept constant for all transitions (corresponding to an assumed constant instrumental resolution). For S $L_{2,3}$, the strongest emission lines are well separated, which allows us to choose the Lorentzian widths separately for each emission line. For N and O K, this is not the case, and – as a simple approximation – Lorentzian widths were chosen to increase linearly towards lower emission energies (to account for variations in the lifetimes of the involved core and valence holes[13]). To align the position of the HOMO (14a') transition with the experimental data at each edge, the calculated spectra needed to be shifted by only small amounts (< 1 eV). The theoretical energy scales for all edges were then stretched by a factor of 1.06 to align with the experiment over the full energy range. For the experimental C K and S $L_{2,3}$ XES spectra, contributions from higher orders of O K (for C K) and C K (for S $L_{2,3}$) emission, excited by higher orders/harmonics of the beamline, were subtracted. The energy axes for O K, C K, and S $L_{2,3}$ were aligned in Figure 1 such that features originating from the same final state are aligned, as also indicated by the dashed vertical lines.

Figure 1. Non-resonant O K (top), C K (center), and S $L_{2,3}$ (bottom) XES spectra of DMSO. Experimental spectra (black) are shown in comparison with DFT-based spectra calculations (blue). The latter are shown as colored vertical lines, illustrating the intensities and energies of the individual valence hole final states (14a' to 7a', as labelled next to the respective lines for O K, C K, and S L_3). Theoretical spectra after broadening with Voigt line profiles are shown as blue continuous lines.

The three spectra give a quite comprehensive picture of the occupied valence orbitals of DMSO, spreading over an energy range of more than 20 eV. Except for a few distinct differences (which will be discussed further below), the calculations are in very good agreement with the experimental spectra. This allows us a detailed assignment of the spectral features and a discussion of the spectral intensities based on the iso-density surfaces in Figure 2 and the Löwdin population analysis[14] of the involved orbitals in Table S1 in the supporting information. The main aspects for this discussion are a suitable local symmetry (p-type for K emission and s- or d-type for $L_{2,3}$ emission) and the overlap of the orbitals at the respective atomic sites.
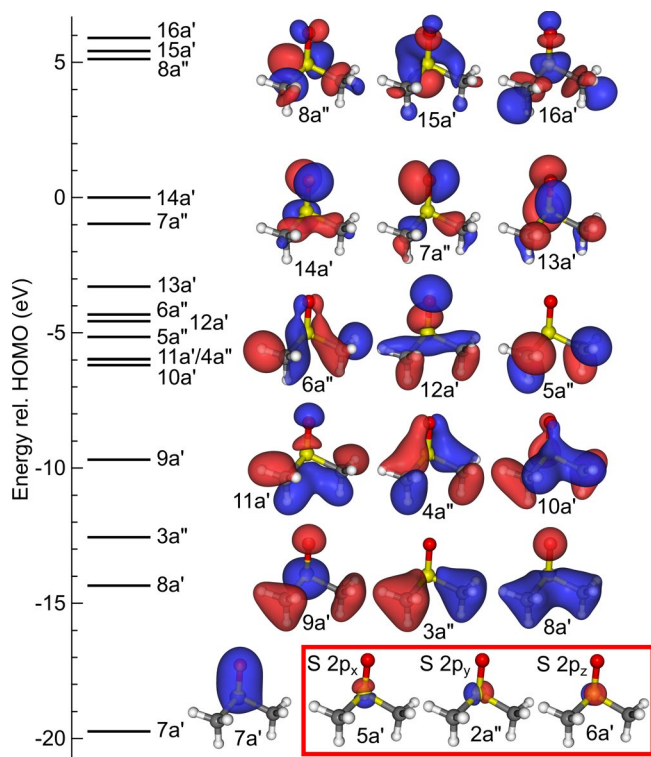
While this is straight-forward for O K and C K XES with a single core level, the situation for S $L_{2,3}$ XES is more complex. In DMSO, the S 2p core levels experience both spin-orbit and molecular-field splitting[15–17]. Since the spin-orbit splitting of ~1.2 eV[18,19] is much larger than the molecular-field splitting ΔE_{MF}, which is ~0.15 eV in our case (see below), mixing of states with different j can be neglected[16] and splitting into three levels, i.e., one $2p_{1/2}$ and two $2p_{3/2}$ levels, is expected. This was discussed in detail by Gel'mukhanov et al. for the S 2p photoemission and $L_{2,3}VV$ Auger spectra of H_2S[15,16], giving the wave functions for the molecular-field split $2p_{3/2}$ levels as a linear combination $\psi = A\left|\frac{3}{2} \pm\frac{3}{2}\right\rangle + B\left|\frac{3}{2} \mp\frac{1}{2}\right\rangle$ of the atomic eigenfunctions $|jm\rangle$, while the wave function $\psi = \left|\frac{1}{2} \pm\frac{1}{2}\right\rangle$ of the $2p_{1/2}$ level is undisturbed[16]. The coefficients A and B, as well as ΔE_{MF}, can be determined analytically as a function of the S 2p ionization potentials $I(S\ 2p_x)$, $I(S\ 2p_y)$, and $I(S\ 2p_z)$, calculated without taking the spin-orbit splitting into account[16]. Using this approach and the ionization potentials from our StoBe calculations, we estimate a molecular-field splitting of $\Delta E_{MF} = 0.15\ eV$ for the S $2p_{3/2}$ levels in DMSO, and derive the wave functions of the $2p_{1/2}$ and $2p_{3/2}$ levels. Using the 2p orbitals without spin-orbit splitting (see iso-density surfaces in

Figure 2) as a basis, we get $\sqrt{3}|2p_{1/2}\rangle = |2p_x\rangle + |2p_y\rangle + |2p_z\rangle$, $|2p_{3/2}\rangle_1 = 0.112|2p_x\rangle + 0.756|2p_y\rangle + 0.645|2p_z\rangle$, and $|2p_{3/2}\rangle_2 = 0.809|2p_x\rangle + 0.308|2p_y\rangle - 0.501|2p_z\rangle$. In Figure 1, the emission intensities for these three core-level hole initial states $|CL\rangle$ and the valence hole final state $|f\rangle$ are then simulated by

$$I_{f,CL} = (h\nu)^3 \left(\sum_{\hat{a}=\hat{x},\hat{y},\hat{z}} |\langle f|\hat{a}|CL\rangle|^2 \right) = (h\nu)^3 \left(\sum_{\hat{a}=\hat{x},\hat{y},\hat{z}} \left| \sum_{b=x,y,z} c_{b,CL} \langle f|\hat{a}|2p_b\rangle \right|^2 \right),$$

with the cartesian components of the dipole matrix elements $\langle f|\hat{a}|2p_b\rangle$ calculated by StoBe, and the coefficients $c_{b,CL}$ given above.

While the experimental resolution for the S $L_{2,3}$ data would be in the range of the expected molecular-field splitting, the sharpest feature in the emission spectra (the 14a' S L_2 emission) has a width of ~0.5 eV, which we attribute to lifetime, inhomogeneous, and – probably dominating – vibronic broadening. In fact, coupling to the symmetric umbrella bend in the methyl moieties was observed for S 2p photoelectron spectroscopy of dimethyl sulfide[20], and it is reasonable to expect that this also happens for S $L_{2,3}$ of DMSO. Thus, the molecular-field splitting is too small to be resolved in the experiment. In contrast, the composition of the core levels in terms of S $2p_x$, $2p_y$, and $2p_z$ does directly influence the spectral intensities, as will be discussed below.

Figure 2. Energy diagram and iso-density surfaces (iso-surface value: $0.05\ e/\text{Å}^3$) of the occupied and three lowest unoccupied ground state valence orbitals of DMSO. The non-relativistic S 2p core orbitals are illustrated in the red box on the bottom right.

In the following, we discuss the contributions of all valence orbitals to the O K, C K, and S $L_{2,3}$ XES spectra, starting with the 14a' orbital (HOMO) and continuing to lower-lying orbitals. We find that the 14a' and 7a" orbitals are dominated by O 2p contributions – in a simplified picture representing the lone-pair orbitals at the oxygen atom – and give rise to the strongest spectral lines in the O K XES at 527.6 and 526.7 eV, respectively. Furthermore, these orbitals also extend to the S and C atoms, including C 2p and S 3s and 3d contributions, and thus corresponding emission lines are also found for C K (281.2 and 280.1 eV) and S $L_{2,3}$ XES (162.6 and 161.3 eV for S L_3).

While the spectral shape and relative intensities of the broadened theory curve gives a good description for C K XES, the HOMO peak in the broadened O K XES calculation appears more intense than in the experimental spectrum. There are several factors that might play a role: first, the calculated spectra are broadened with symmetric profiles, while some asymmetry can be expected due to vibrational broadening. This could shift some intensity of the 14a' line to lower emission energies, lowering the intensity of the highest-energy peak at 527.5 eV while increasing that of the peak at 526.6 eV. Second, the calculations were performed for an isolated DMSO molecule, while the experiment probes liquid DMSO. In the latter, some influence of the neighboring molecules is expected, in particular for the O lone pairs participating in hydrogen bonding, as has been studied for DMSO/water mixtures[9].
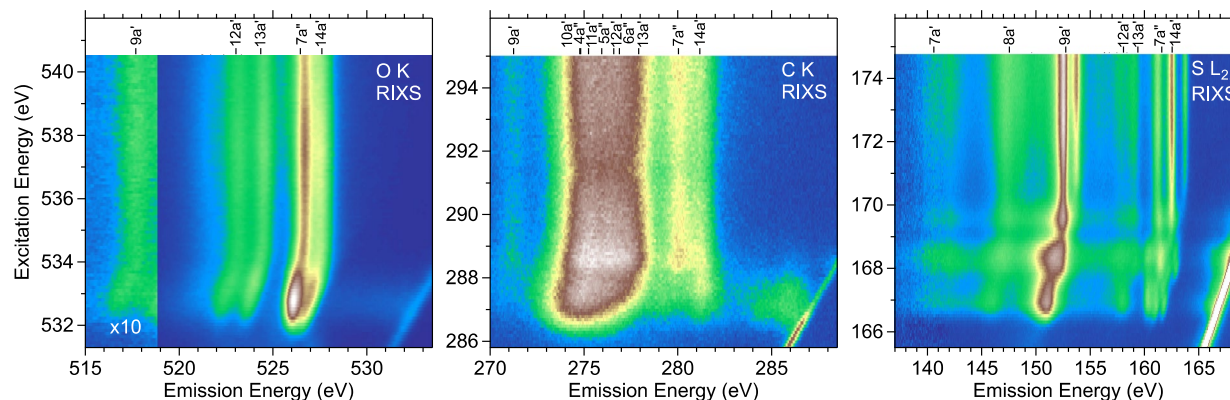
For S $L_{2,3}$, the situation is interesting: emission involving the 14a' orbital gives only significant intensity with $\left|2p_{3/2}\right\rangle_2$ or $\left|2p_{1/2}\right\rangle$ initial states, while nearly no intensity is expected for $\left|2p_{3/2}\right\rangle_1$. The situation is then reversed for 7a", with emission mainly involving $\left|2p_{3/2}\right\rangle_1$. We note that the 7a" intensity is underestimated in the calculation, which might be caused by the interaction with neighboring molecules not included in the calculation.

13a' and 12a' again exhibit significant O 2p contributions, leading to the two prominent O K emission lines at 524.5 and 523.2 eV. These orbitals also have C 2p contributions, and the calculation thus predicts significant contribution for the C K emission as well. In contrast, they only have small admixtures of S 3s and 3d, and the corresponding lines are very weak in the S L_3 emission; however, they are still visible, since they are well separated from any other line with larger emission intensity. 6a", as well as 5a" through 10a', are dominated by C 2p contributions with very small overlap with the O atom and no S 3s or 3d contributions. Consequently, the

corresponding lines are very strong for C K XES, while they lead to only weak (but distinctive) features in the O K and S L_3 XES.

The main contribution to the 9a' orbital is from S 3s, leading to the most prominent S $L_{2,3}$ emission lines at 152.6 and 153.8 eV. Since this orbital is well separated from the others and has some minor O 2p and C 2p contributions, we can also identify corresponding peaks in the C K and O K XES. The 3a" orbital is mainly derived from C 2s and has no overlap and/or the wrong symmetry to lead to an emission line in any of the three spectra. Finally, 8a' and 7a' have significant S 3s character, giving two distinct emission lines in the S $L_{2,3}$ XES. 7a' also has some O 2p admixture, leading to a weak emission line in the O K XES.

We note some (weak) intensity in the experimental S $L_{2,3}$ XES around 150.5 eV, which has no counterpart in the calculated spectrum. This feature can likely be attributed to "semi-Auger" satellites, which we have previously observed in the S $L_{2,3}$ emission of alkaline earth metal sulfides[21].
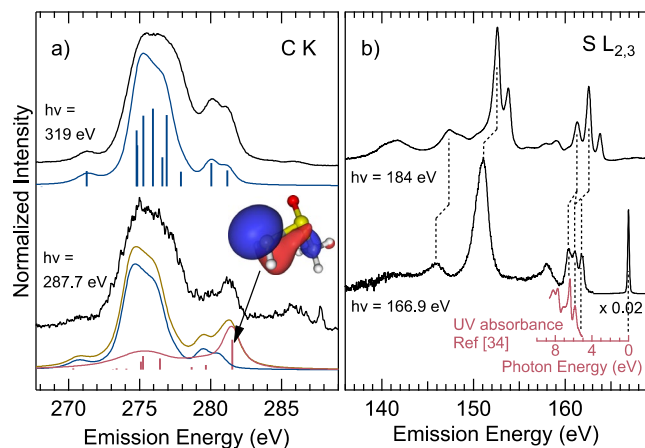

Figure 3. O K (left), C K (center), and S $L_{2,3}$ (right) RIXS maps of liquid DMSO. The emission intensity is shown color-coded from blue (low intensity) to white (high intensity) as a function of

emission and excitation energies. Above the maps, emission lines are labeled and marked according to their calculated non-resonant emission energies.

In Figure 3, the RIXS maps at the O K, C K, and S $L_{2,3}$ edges are shown. For the S $L_{2,3}$ map, contributions from 2nd order C K emission excited by higher orders/harmonics of the beamline have been subtracted. Emission lines are labeled at the top of each map using the calculated non-resonant emission energies. Along the excitation energy direction (ordinate), the map can be divided into three regions: (1) below the absorption edge, where no emission and only elastically scattered photons (at equal excitation and emission energies) are found, (2) the area at and a few eV above the absorption edge, where significant changes of emission line energies and intensities are observed as a function of excitation energy, and (3) the area at higher excitation energies, where the emission lines do not shift and the spectra are very similar to the non-resonant spectra presented in Figure 1. Along the emission energy direction (abscissa), we can distinguish between the participant region, including and just below the elastic line, and the spectator region at even lower emission energies.

In all three maps, we observe significant shifts of the emission lines around the absorption edge, caused by the interaction between the excited electron in one of the LUMO levels ("spectator") and the final state valence hole; such shifts are often referred to as "spectator shifts"[22,23]. They are strongest for S $L_{2,3}$ (up to 1.4 eV) and weakest for C K RIXS.

Figure 4. a) Experimental C K spectra of DMSO with non-resonant (XES, $hv_{exc.} = 319\ eV$) and resonant (RIXS, $hv_{exc.} = 287.7\ eV$) excitation (black), in comparison with calculations for DMSO (blue) and DMSO minus one proton, i.e., $CH_3SOCH_2^-$ (red, see text). The iso-density surface (iso-surface value: $0.05\ e/\text{Å}^3$) of the HOMO of $CH_3SOCH_2^-$ is also shown. b) Experimental S $L_{2,3}$ spectrum at non-resonant (XES, $hv_{exc.} = 184\ eV$) and S L_3 spectrum at resonant (RIXS, $hv_{exc.} = 166.9\ eV$) excitation (black), in comparison with the UV absorbance spectrum of DMSO digitized from[24] (red).
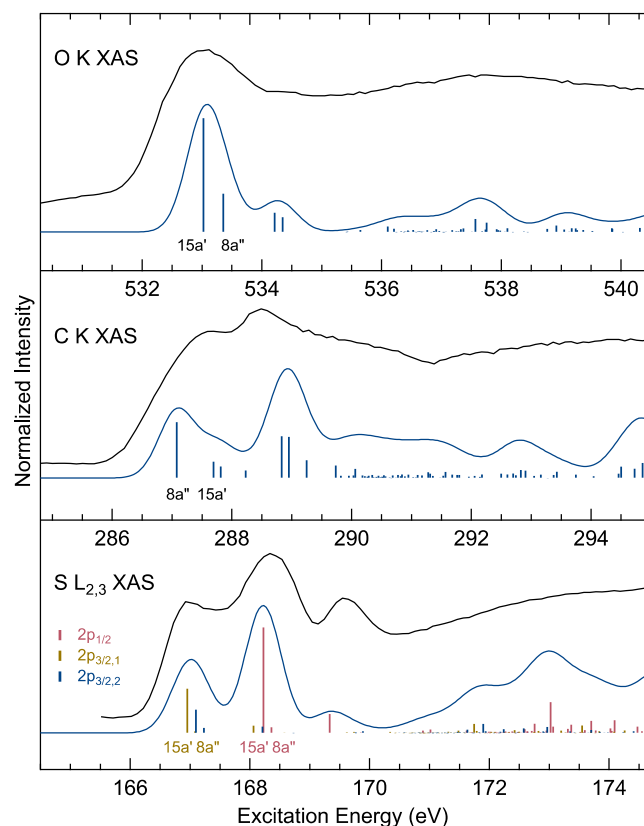
In the participant region, we find loss signals close to the elastic line at all absorption edges, which can be attributed to vibrational excitations. Relative to the elastic line, these features have low intensity for O K and S $L_{2,3}$, while they are much more intense for C K, where strong coupling to the vibrational modes of the –CH₃ moieties occurs. This is expected, since the nuclear dynamics on the time scale of the core-hole lifetime that give rise to the coupling[25–27] will be stronger for the (light) protons at this functional group. A closer look at the excitation energy region around $hv_{exc.} = 287.7\ eV$, with strong vibrational loss intensity, reveals a significant increase of the relative intensity of the emission line at $hv_{em.} = 281.2\ eV$ compared to the non-resonant spectrum,

as is also visible in Figure 4 a). Such changes in relative intensities as a function of excitation energy can be caused by the angular anisotropy of the x-ray emission process[28] for molecules. The linear polarization of the exciting photons (in the plane of the storage ring) can only excite orbitals (and consequently molecules) of suitable orientation. For processes, in which the molecule does not move significantly before emission takes place, this leads to an angular anisotropy of the *emission* as well, depending on the symmetry of the involved molecular orbitals. For DMSO, a significant effect of the angular anisotropy was found at the O K edge[10]. However, for the experimental geometry in our experiment with an angle of 45° between the polarization vector of the exciting photons and the direction of the outgoing photons, an anisotropy effect of only 15% is predicted when using the formalism of Luo et al.[28], which will be further reduced by some movement of the molecules on the time scale of the RIXS process. Instead, we thus attribute the increased intensity at $hv_{em.} = 281.2\ eV$ to nuclear dynamics in the core-excited state, leading to the full removal of one of the protons. As an approximate model for the fully dissociated state, we have calculated the C K XES spectrum of DMSO minus one proton, i.e., $CH_3SOCH_2^-$, which is shown in red in Figure 4 a). Removing a proton from the –CH$_3$ group changes the orbital structure, with the new HOMO orbital now dominated by the remaining lone pair electrons at the $-CH_2^-$ moiety (see iso-density surface in Figure 4 a), which gives rise to the strongest peak of the spectrum (red). In a rough approximation, the experimental spectrum can then be described as a weighted sum of the calculated (non-resonant) spectrum of DMSO (representing processes *without* dissociation) and that of $CH_3SOCH_2^-$ (representing processes *with* dissociation), which is shown in gold in Figure 4 a) and gives a good description of the experimental spectrum.

For S L$_{2,3}$ RIXS, significant spectral changes can be observed as a function of excitation energy. As discussed above, strong spectator shifts are observed, which is illustrated by dashed lines in

Figure 4 b), where the non-resonant S $L_{2,3}$ spectrum is compared with the S L_3 spectrum resonantly excited at 166.9 eV. In addition to the shifts, a significant broadening of the 9a' emission line is observed for resonant excitation. This could be caused by stronger lifetime broadening of this particular final state, an increased vibronic coupling, and/or an overlap of different close-lying final state configurations, with the spectator electron in different formerly unoccupied valence states.

In the emission energy region between 159 and 163 eV, where emission with final state holes in the 14a' and 7a" is expected, we find three distinct features for excitation at $hv_{exc.} = 166.9\ eV$. At this energy, we expect very closely lying resonances involving the 8a" and 15a' orbitals (see also discussion of Figure 5 below) that are expected to strongly overlap if vibrational broadening is included. This gives a total of 4 possible electronic final states. Discussing this in an energy-loss picture, we compare with the UV absorbance spectrum of DMSO[24] (shown in red in Figure 4 b)). The electronic initial and final states are the same for RIXS and UV absorption and, disregarding nuclear dynamics in the RIXS process, energetics are expected to be very similar. In the energy-loss picture, we have thus aligned the 0 of the energy scale of the absorption spectrum with the elastic line of the RIXS spectrum and find a good agreement between the energy positions in RIXS and UV absorption, as indicated by the dashed lines. In contrast, the relative intensities are very different, which is expected by the different transition matrix elements involved (Kramers-Heisenberg formalism for RIXS and Fermi's golden rule for UV absorption). We tentatively assign the lowest-energy emission line at 160.4 eV to the $(7a")^{-1}(8a")^1$ final state, the center line at 161.0 eV to $(7a")^{-1}(15a')^1$ or $(14a')^{-1}(8a")^1$ final states, and the highest-energy emission line at 161.8 eV to the $(14a')^{-1}(15a')^1$ final state.

Figure 5. O K, C K, and S $L_{2,3}$ partial fluorescence yield XAS spectra (black), extracted from the RIXS maps in Figure 3, in comparison with calculated XAS spectra. Colored vertical lines represent energies and intensities of individual transitions, while the blue curves show the calculations broadened by a Gaussian with a full width of half maximum of 0.7 eV. Below the two lowest transitions, the corresponding (ground state) orbital assignment is given.

Figure 5 shows partial fluorescence yield (PFY) XAS spectra, extracted from the maps in Figure 3 by integrating the emission intensity over the entire emission energy range of each RIXS map (excluding the elastic line). Calculated spectra are shown for comparison. For S $L_{2,3}$ XAS, spectra were simulated in an analogous way as for XES. Depending on the edge, the calculations indicate changes in the energetic order of the orbitals involved in the two lowest absorption resonances: For O K and S $L_{2,3}$ XAS, the first resonance involves the 14a' and the second resonance the 8a''

orbitals, while this is reversed for C K XAS. The calculated spectra qualitatively reproduce the spectral features of the experimental spectra, but some relative intensities are different. In particular, spectral features are better defined for the calculation, which can be attributed to vibrational envelopes present in the experiment but not included in the calculation, as well as saturation effects that often affect XAS spectra collected with PFY.

In summary, the complete electronic structure of liquid DMSO has been investigated using RIXS at the O K, C K, and S $L_{2,3}$ edges. By comparing to DFT-based spectra calculations, the data allows a local and symmetry-resolved analysis of the orbital structure of DMSO. The calculated molecular orbitals are analyzed in terms of their atom- and symmetry-resolved Löwdin gross populations. We find some orbitals mostly located at individual atoms, while others are delocalized over several atoms or the entire molecule. The analysis of the S $L_{2,3}$ XES spectra requires to take molecular-field splitting of the S 2p levels into account, which strongly influences the relative intensities involving the $2p_{1/2}$ and molecular-field split $2p_{3/2}$ levels. The RIXS maps at all three absorption edges exhibit significant spectator shifts as a function of excitation energy. Furthermore, we find strong vibronic coupling and the ultra-fast removal of a proton on the timescale of the RIXS process for excitation at the $-CH_3$ moieties of the molecule. We describe this in a simplified computational model, which can serve as an approach for other molecular systems without the need for an explicit molecular dynamics treatment.

METHODS

Pure liquid DMSO (99% purity, purchased from VWR) was measured with RIXS and XES using the flow-through liquid cell of our Solid and Liquid Spectroscopic Analysis (SALSA) endstation[29] at beamline 8.0.1 of the ALS. The high transmission of SALSA's variable line space grating soft

x-ray spectrometer[30] allows to collect full RIXS maps, where the x-ray emission intensity is color-coded as a function of excitation and emission energies[30–32]. During the measurements, the DMSO sample was continuously pumped through the liquid cell, replacing the probed volume several hundred times per second. In SALSA, the liquid is separated from the vacuum of the experimental station by thin (~100 nm) membranes made from Si_3N_4 (for the O and C K edges; SILSON) or amorphous carbon (for the S $L_{2,3}$ edge; JAVU AB). We routinely monitor for spectral contributions of molecular fragments that might deposit on the membranes during the measurements but could not find any such contributions during the DMSO experiments reported here. The emission and excitation energy scales were calibrated using the prominent features of the O K XES spectrum of liquid water and the elastically scattered peak, respectively, as described in the Supplementary Information.

The XES and XAS spectra at the C K, O K, and S $L_{2,3}$ edges of an isolated DMSO molecule were calculated using the StoBe-DeMon package[33]. The modified generalized gradient approximation (GGA) exchange and correlation functionals of Becke and Perdew[34–36] and double-zeta (for hydrogen) and triple-zeta (for carbon, oxygen, and sulfur)[37] bases were employed for geometry optimization and single-point calculations. For core-excited atoms, diffuse IGLO-III basis sets[38] were used. XAS and XES transition probabilities were calculated by the half core-hole transition potential method[39] or based on the ground-state, respectively. The transition energies were calculated with a Δ(Kohn–Sham self-consistent field) approach that includes differential relativistic effects associated with the removal of one electron from the 1s orbital[39]. In the case of the C emission, the role of the two indistinguishable carbon atoms needs to be briefly discussed. In the gas phase, the core hole would delocalize over the two carbon sites and an interference term for the cross section would need to be considered[27,40]. For liquid DMSO (as in our study), we do

not need to include this interference term, since the symmetry is (slightly) broken, thus localizing the core hole at one of the two sites.

ASSOCIATED CONTENT

Supporting Information.

The following files are available free of charge.

Description of the energy calibration procedure, molecular structure of DMSO, and Löwdin population analysis of the orbitals of DMSO (PDF)

REFERENCES

(1) Chesnut, D. B.; Quin, L. D. Nature of Bonding in the Sulfuryl Group. *Journal of Computational Chemistry* **2004**, *25* (5), 734–738. https://doi.org/10.1002/jcc.20003.
(2) Clark, T.; Murray, J. S.; Lane, P.; Politzer, P. Why Are Dimethyl Sulfoxide and Dimethyl Sulfone Such Good Solvents? *J Mol Model* **2008**, *14* (8), 689–697. https://doi.org/10.1007/s00894-008-0279-y.
(3) Wen, Y.-C.; Kuo, H.-C.; Jia, H.-W. Multinuclear NMR Spectroscopy for Differentiation of Molecular Configurations and Solvent Properties between Acetone and Dimethyl Sulfoxide. *Journal of Molecular Structure* **2016**, *1109*, 154–160. https://doi.org/10.1016/j.molstruc.2016.01.004.
(4) Onthong, U.; Megyes, T.; Bakó, I.; Radnai, T.; Grósz, T.; Hermansson, K.; Probst, M. X-Ray and Neutron Diffraction Studies and Molecular Dynamics Simulations of Liquid DMSO. *Phys. Chem. Chem. Phys.* **2004**, *6* (9), 2136–2144. https://doi.org/10.1039/B311027C.
(5) Reuter, H. Structural Parameters of Dimethyl Sulfoxide, DMSO, at 100 K, Based on a Redetermination by Use of High-Quality Single-Crystal X-Ray Data. *Acta Crystallographica Section E Crystallographic Communications* **2017**, *73* (10), 1405–1408. https://doi.org/10.1107/S2056989017012464.

(6)   Sze, K. H.; Brion, C. E.; Tronc, M.; Bodeur, S.; Hitchcock, A. P. Inner and Valence Shell Electronic Excitation of Dimethyl Sulfoxide by Electron Energy Loss and Photoabsorption Spectroscopies. *Chemical Physics* **1988**, *121* (2), 279–297. https://doi.org/10.1016/0301-0104(88)90034-1.

(7)   Vogt, L. I.; Cotelesage, J. J. H.; Dolgova, N. V.; Titus, C. J.; Sharifi, S.; George, S. J.; Pickering, I. J.; George, G. N. X-Ray Absorption Spectroscopy of Organic Sulfoxides. *RSC Adv.* **2020**, *10* (44), 26229–26238. https://doi.org/10.1039/D0RA04653A.

(8)   Atak, K.; Engel, N.; Lange, K. M.; Golnak, R.; Gotz, M.; Soldatov, M.; Rubensson, J.-E.; Kosugi, N.; Aziz, E. F. The Chemical Bond in Carbonyl and Sulfinyl Groups Studied by Soft X-Ray Spectroscopy and Ab Initio Calculations. *ChemPhysChem* **2012**, *13* (13), 3106–3111. https://doi.org/10.1002/cphc.201200314.

(9)   Engel, N.; Atak, K.; Lange, K. M.; Gotz, M.; Soldatov, M.; Golnak, R.; Suljoti, E.; Rubensson, J.-E.; Aziz, E. F. DMSO–Water Clustering in Solution Observed in Soft X-Ray Spectra. *J. Phys. Chem. Lett.* **2012**, *3* (24), 3697–3701. https://doi.org/10.1021/jz301665s.

(10)   Dierker, B.; Suljoti, E.; Atak, K.; Lange, K. M.; Engel, N.; Golnak, R.; Dantz, M.; Hodeck, K.; Khan, M.; Kosugi, N.; Aziz, E. F. Probing Orbital Symmetry in Solution: Polarization-Dependent Resonant Inelastic Soft x-Ray Scattering on Liquid Micro-Jet. *New J. Phys.* **2013**, *15* (9), 093025. https://doi.org/10.1088/1367-2630/15/9/093025.

(11)   Takamuku, T.; Tokuda, T.; Uchida, T.; Sonoda, K.; Marekha, B. A.; Idrissi, A.; Takahashi, O.; Horikawa, Y.; Matsumura, J.; Tokushima, T.; Sakurai, H.; Kawano, M.; Sadakane, K.; Iwase, H. Hydrogen Bonds of the Imidazolium Rings of Ionic Liquids with DMSO Studied by NMR, Soft X-Ray Spectroscopy, and SANS. *Phys. Chem. Chem. Phys.* **2018**, *20* (18), 12858–12869. https://doi.org/10.1039/C8CP00963E.

(12)   Nagasaka, M. Site Selective Analysis of Water in Hydrogen Bond Network of Aqueous Dimethyl Sulfoxide Solutions by Oxygen K-Edge X-Ray Absorption Spectroscopy. *Journal of Molecular Liquids* **2022**, *366*, 120310. https://doi.org/10.1016/j.molliq.2022.120310.

(13)   Weinhardt, L.; Fuchs, O.; Umbach, E.; Heske, C.; Fleszar, A.; Hanke, W. Resonant Inelastic Soft X-Ray Scattering, x-Ray Absorption Spectroscopy, and Density Functional Theory Calculations of the Electronic Bulk Band Structure of CdS. *Phys. Rev. B* **2007**, *75* (16), 165207. https://doi.org/10.1103/PhysRevB.75.165207.

(14)   Löwdin, P. On the Non-Orthogonality Problem Connected with the Use of Atomic Wave Functions in the Theory of Molecules and Crystals. *The Journal of Chemical Physics* **1950**, *18* (3), 365–375. https://doi.org/10.1063/1.1747632.

(15)   Svensson, S.; Ausmees, A.; Osborne, S. J.; Bray, G.; Gel'mukhanov, F.; Ågren, H.; Naves de Brito, A.; Sairanen, O.-P.; Kivimäki, A.; Nõmmiste, E.; Aksela, H.; Aksela, S. Observation of an Anomalous Decay Ratio between the Molecular Field Split Levels in the S 2p Core Photoelectron and LVV Auger Spectrum of H_2S. *Phys. Rev. Lett.* **1994**, *72* (19), 3021–3024. https://doi.org/10.1103/PhysRevLett.72.3021.

(16)   Gel'mukhanov, F.; Ågren, H.; Svensson, S.; Aksela, H.; Aksela, S. Theory of Auger Spectra for Molecular-Field-Split Core Levels. *Phys. Rev. A* **1996**, *53* (3), 1379–1387. https://doi.org/10.1103/PhysRevA.53.1379.

(17)   Børve, K. J. On the Calculation of Molecular Field Splitting in S 2p Photoelectron Spectra. *Chemical Physics Letters* **1996**, *262* (6), 801–806. https://doi.org/10.1016/S0009-2614(96)01141-4.

(18)	Durbin, T. D.; Lince, J. R.; Didziulis, S. V.; Shuh, D. K.; Yarmoff, J. A. Soft X-Ray Photoelectron Spectroscopy Study of the Interaction of Cr with $MoS_2(0001)$. *Surface Science* **1994**, *302* (3), 314–328. https://doi.org/10.1016/0039-6028(94)90836-2.

(19)	Mullins, D. R.; Lyman, P. F.; Overbury, S. H. Interaction of S with W(001). *Surface Science* **1992**, *277* (1), 64–76. https://doi.org/10.1016/0039-6028(92)90612-A.

(20)	Børve, K. J.; Sæthre, L. J.; Svensson, S. Molecular-Field Splitting in S2p Photoelectron Spectra of Dimethyl Sulfide and Sulfur Dichloride. *Chemical Physics Letters* **1999**, *310* (5), 439–444. https://doi.org/10.1016/S0009-2614(99)00825-8.

(21)	Weinhardt, L.; Hauschild, D.; Fuchs, O.; Steininger, R.; Jiang, N.; Blum, M.; Denlinger, J. D.; Yang, W.; Umbach, E.; Heske, C. Satellite-Dominated Sulfur $L_{2,3}$ X-Ray Emission of Alkaline Earth Metal Sulfides. *ACS Omega* **2023**, *8* (5), 4921–4927. https://doi.org/10.1021/acsomega.2c07228.

(22)	Ågren, H.; Luo, Y.; Gelmukhanov, F.; Jensen, H. J. Aa. Screening in Resonant X-Ray Emission of Molecules. *J. Electr. Spectr. Rel. Phenom.* **1996**, *82* (1–2), 125. https://doi.org/10.1016/S0368-2048(96)03041-1.

(23)	Weinhardt, L.; Benkert, A.; Meyer, F.; Blum, M.; Wilks, R. G.; Yang, W.; Bär, M.; Reinert, F.; Heske, C. Nuclear Dynamics and Spectator Effects in Resonant Inelastic Soft X-Ray Scattering of Gas-Phase Water Molecules. *J. Chem. Phys.* **2012**, *136* (14), 144311. https://doi.org/doi:10.1063/1.3702644.

(24)	Gollnick, K.; Stracke, H.-U. Direct and Sensitized Photolysis of Dimethyl Sulphoxide in Solution. *Pure Appl. Chem.* **1973**, *33* (2), 217–246. https://doi.org/10.1351/pac197333020217.

(25)	Hennies, F.; Polyutov, S.; Minkov, I.; Pietzsch, A.; Nagasono, M.; Ågren, H.; Triguero, L.; Piancastelli, M.-N.; Wurth, W.; Gel'mukhanov, F.; Föhlisch, A. Dynamic Interpretation of Resonant X-Ray Raman Scattering: Ethylene and Benzene. *Phys. Rev. A* **2007**, *76* (3), 032505. https://doi.org/10.1103/PhysRevA.76.032505.

(26)	Weinhardt, L.; Weigand, M.; Fuchs, O.; Bär, M.; Blum, M.; Denlinger, J. D.; Yang, W.; Umbach, E.; Heske, C. Nuclear Dynamics in the Core-Excited State of Aqueous Ammonia Probed by Resonant Inelastic Soft x-Ray Scattering. *Phys. Rev. B* **2011**, *84* (10), 104202. https://doi.org/10.1103/PhysRevB.84.104202.

(27)	Gel'mukhanov, F.; Odelius, M.; Polyutov, S. P.; Föhlisch, A.; Kimberg, V. Dynamics of Resonant X-Ray and Auger Scattering. *Rev. Mod. Phys.* **2021**, *93* (3), 035001. https://doi.org/10.1103/RevModPhys.93.035001.

(28)	Luo, Y.; Ågren, H.; Gel'mukhanov, F. Polarization Anisotropy in Resonant X-Ray Emission from Molecules. *Phys. Rev. A* **1996**, *53* (3), 1340. https://doi.org/10.1103/PhysRevA.53.1340.

(29)	Blum, M.; Weinhardt, L.; Fuchs, O.; Bär, M.; Zhang, Y.; Weigand, M.; Krause, S.; Pookpanratana, S.; Hofmann, T.; Yang, W.; Denlinger, J. D.; Umbach, E.; Heske, C. Solid and Liquid Spectroscopic Analysis (SALSA) - a Soft x-Ray Spectroscopy Endstation with a Novel Flow-through Liquid Cell. *Rev. Sci. Instrum.* **2009**, *80* (12), 123102. https://doi.org/10.1063/1.3257926.

(30)	Fuchs, O.; Weinhardt, L.; Blum, M.; Weigand, M.; Umbach, E.; Bär, M.; Heske, C.; Denlinger, J.; Chuang, Y. D.; McKinney, W.; Hussain, Z.; Gullikson, E.; Jones, M.; Batson, P.; Nelles, B.; Follath, R. High-Resolution, High-Transmission Soft x-Ray Spectrometer for the Study of Biological Samples. *Rev. Sci. Instrum.* **2009**, *80* (6), 63103. https://doi.org/10.1063/1.3133704.

(31)   Fuchs, O.; Zharnikov, M.; Weinhardt, L.; Blum, M.; Weigand, M.; Zubavichus, Y.; Bär, M.; Maier, F.; Denlinger, J. D.; Heske, C.; Grunze, M.; Umbach, E. Comment on "Isotope and Temperature Effects in Liquid Water Probed by X-Ray Absorption and Resonant X-Ray Emission Spectroscopy" - Fuchs et al. Reply. *Phys. Rev. Lett.* **2008**, *100* (24), 249802. https://doi.org/10.1103/PhysRevLett.100.249802.

(32)   Weinhardt, L.; Fuchs, O.; Fleszar, A.; Bär, M.; Blum, M.; Weigand, M.; Denlinger, J. D.; Yang, W.; Hanke, W.; Umbach, E.; Heske, C. Resonant Inelastic Soft X-Ray Scattering of CdS: A Two-Dimensional Electronic Structure Map Approach. *Phys. Rev. B* **2009**, *79* (16), 165305. https://doi.org/10.1103/PhysRevB.79.165305.

(33)   Hermann, K.; Pettersson, L. G. M.; Casida, M. E.; Daul, C.; Goursot, A.; Koester, A.; Proynov, E.; St-Amant, A.; Salahub, D. R. Contributing Authors: Carravetta, V.; Duarte, H.; Friedrich, C.; Godbout, N.; Guan, J.; Jamorski, C.; Leboeuf, M.; Leetmaa, M.; Nyberg, M.; Patchkovskii, S.; Pedocchi, L.; Sim, F.; Triguero, L.; Vela, A. StoBe-deMon Version 3.1 (2011).

(34)   Becke, A. D. Density-Functional Exchange-Energy Approximation with Correct Asymptotic Behavior. *Phys. Rev. A* **1988**, *38* (6), 3098–3100. https://doi.org/10.1103/PhysRevA.38.3098.

(35)   Perdew, J. P. Density-Functional Approximation for the Correlation Energy of the Inhomogeneous Electron Gas. *Phys. Rev. B* **1986**, *33* (12), 8822–8824. https://doi.org/10.1103/PhysRevB.33.8822.

(36)   Perdew, J. P. Erratum: Density-Functional Approximation for the Correlation Energy of the Inhomogeneous Electron Gas. *Phys. Rev. B* **1986**, *34* (10), 7406–7406. https://doi.org/10.1103/PhysRevB.34.7406.

(37)   Godbout, N.; Salahub, D. R.; Andzelm, J.; Wimmer, E. Optimization of Gaussian-Type Basis Sets for Local Spin Density Functional Calculations. Part I. Boron through Neon, Optimization Technique and Validation. *Can. J. Chem.* **1992**, *70* (2), 560–571. https://doi.org/10.1139/v92-079.

(38)   Kutzelnigg, W.; Fleischer, U.; Schindler, M. *The IGLO-Method: Ab-Initio Calculation and Interpretation of NMR Chemical Shifts and Magnetic Susceptibilities". En. Deuterium and Shift Calculation. NMR Basic Principles and Progress*; Springer: Heidelberg, 1990.

(39)   Triguero, L.; Pettersson, L. G. M.; Ågren, H. Calculations of Near-Edge x-Ray-Absorption Spectra of Gas-Phase and Chemisorbed Molecules by Means of Density-Functional and Transition-Potential Theory. *Phys. Rev. B* **1998**, *58* (12), 8097–8110. https://doi.org/10.1103/PhysRevB.58.8097.

(40)   Gel'mukhanov, F.; Ågren, H. Resonant Inelastic X-Ray Scattering with Symmetry-Selective Excitation. *Phys. Rev. A* **1994**, *49* (6), 4378–4389. https://doi.org/10.1103/PhysRevA.49.4378.